

Noise evaluation and optimization for a cryogenic sapphire oscillator with 10^{-15} level stability

Encai Zhong(钟恩才), Yan Zheng(郑琰), Hongli Liu(刘洪力), Mingming Liu(刘明明), Jinxu Hong(洪金旭), Yijun Luo(罗逸骏), Ke Deng(邓科), Jie Zhang(张洁), and Zehuang Lu(陆泽晃)

Citation: Chin. Phys. B, 2026, 35 (**7**): 070601. DOI: 10.1088/1674-1056/ae53ba
http://cpb.iphy.ac.cn; http://iopscience.iop.org/cpb

What follows is a list of articles you may be interested in

Physics package based on intracavity laser cooling ^{87}Rb atoms for space cold atom microwave clock

Siminda Deng(邓思敏达), Wei Ren(任伟), Jingfeng Xiang(项静峰), Jianbo Zhao(赵剑波), Lin Li(李琳), Di Zhang(张迪), Jinyin Wan(万金银), Yanling Meng(孟艳玲), Xiaojun Jiang(蒋小军), Tang Li(李唐), Liang Liu(刘亮), and Desheng Lü(吕德胜)

Chin. Phys. B, 2024, 33 (**7**): 070602. DOI: 10.1088/1674-1056/ad4bc1

A redundant subspace weighting procedure for clock ensemble

Hai Xu(徐海), Yu Chen(陈煜), Mo-Chi Liu(刘默驰), and Yu-Zhuo Wang(王玉琢)

Chin. Phys. B, 2024, 33 (**4**): 040601. DOI: 10.1088/1674-1056/ad1b43

Robust free-space optical frequency transfer in time-varying link distances conditions

Zhou Tong(童周), Lei Liu(刘雷), Jia-Liang Wang(王家亮), Qian Cao(操前), Zhi-Cheng Jin(金志成), Kang Ying(应康), Shen-Sheng Han(韩申生), Zheng-Fu Han(韩正甫), and You-Zhen Gui(桂有珍)

Chin. Phys. B, 2024, 33 (**2**): 020601. DOI: 10.1088/1674-1056/ad0718

Ramsey-coherent population trapping Cs atomic clock based on lin||lin optical pumping with dispersion detection

Peng-Fei Cheng(程鹏飞), Jian-Wei Zhang(张建伟), Li-Jun Wang(王力军)

Chin. Phys. B, 2019, 28 (**7**): 070601. DOI: 10.1088/1674-1056/28/7/070601

Noise analysis of grating-based x-ray differential phase-contrast imaging with angular signal radiography

Wali Faiz, Yuan Bao(鲍园), Kun Gao(高昆), Zhao Wu(吴朝), Chen-Xi Wei(卫晨希), Gui-Bin Zan(昝贵彬), Pei-Ping Zhu(朱佩平), Yang-Chao Tian(田扬超)

Chin. Phys. B, 2017, 26 (**4**): 040602. DOI: 10.1088/1674-1056/26/4/040602

INSTRUMENTATION AND MEASUREMENT

Noise evaluation and optimization for a cryogenic sapphire oscillator with 10^{-15} level stability

Encai Zhong(钟恩才)[1,2], Yan Zheng(郑琰)[1,2], Hongli Liu(刘洪力)[1,2], Mingming Liu(刘明明)[1,2], Jinxu Hong(洪金旭)[1,2], Yijun Luo(罗逸骏)[1,2], Ke Deng(邓科)[1,2], Jie Zhang(张洁)[1,2], and Zehuang Lu(陆泽晃)[1,2,†]

[1] *National Gravitation Laboratory, Huazhong University of Science and Technology, Wuhan* 430074, *China*
[2] *School of Physics, Huazhong University of Science and Technology, Wuhan* 430074, *China*

(Received 3 February 2026; revised manuscript received 11 March 2026; accepted manuscript online 18 March 2026)

Cryogenic sapphire oscillators (CSOs) simultaneously achieve ultra-low phase noise and outstanding frequency stability, making them widely used in precision measurement applications. In this study, performance evaluation and noise analysis are conducted on a home-built CSO. When compared with an optically generated microwave (OGM) reference, its synthesized 100 Hz signal demonstrates a relative frequency instability (Allan deviation) of 2.1×10^{-15} at an averaging time of 70 s. After evaluation of the dominant noise sources, it is shown that the short-term frequency stability is limited by the 1.4 Hz vibrational noise from the pulse cryocooler, resulting in a limitation of $1.2 \times 10^{-15}\ \tau^{-1}$. At an averaging time of 100 s, the contribution of temperature fluctuation noise becomes prominent, limiting the frequency stability to 10^{-16}. In the long term, the stability of the voltage reference in the microwave power servo becomes the limiting factor. This research provides guidelines for the development of improved CSOs and their further applications in precision measurement physics.

Keywords: cryogenic sapphire oscillator, noise analysis, frequency stability

PACS: 06.30.Ft, 84.30.Ng, 07.05.Fb

DOI: 10.1088/1674-1056/ae53ba **CSTR:** 32038.14.CPB.ae53ba

1. Introduction

A defining characteristic of ultra-stable microwave signal sources is their exceptionally high frequency stability, which is typically quantified in the time domain using the Allan deviation of relative frequency fluctuations. Currently, the primary methods for generating such ultra-stable microwave signals are the optical frequency division scheme based on frequency-stabilized lasers and cryogenic sapphire oscillators (CSOs).[1–5] Microwave signals produced by these two approaches achieve fractional frequency instability at the level of 10^{-15} to 10^{-16} for one-second averaging times.[6,7] For a 10 GHz carrier, this corresponds to an absolute frequency fluctuation of a few to tens of microhertz. Benefiting from such high frequency resolution, a key application of ultra-stable microwave sources is serving as the local oscillator for cesium fountain clocks.[8] They are used to precisely measure clock transition frequencies, thereby pushing the frequency stability of microwave clocks to the mid-10^{-14} level and beyond.[9,10]

Distinct from the ultra-stable microwave signals derived from lasers stabilized on Fabry–Perot cavities, the resonator of a CSO exhibits a frequency-temperature turning point (FTTP),[11] which grants it superior medium- to long-term frequency stability. Moreover, as an all-microwave system, it offers significant advantages in terms of development cost and operational simplicity. As a result, CSOs can serve as frequency references in very long baseline interferometry (VLBI),[12] where their performance rivals that of active hydrogen masers, maintaining data coherence over extended averaging times in deep-space observations. Furthermore, compared to conventional laboratory signal sources, the exceptionally pure signal generated by a CSO is also suitable for quantum computing operations, as it is less likely to disrupt system coherence during qubit manipulation.[13] The cylindrical design of the sapphire resonator enables electromagnetic waves to propagate in a whispering-gallery mode within the sapphire crystal. This property allows it to function as a sensor for testing Lorentz symmetry violation and as a detector for dark matter.[14,15]

To measure the frequency stability of a CSO, it is necessary to employ an additional reference source with better frequency stability,[7] or to use a three-cornered hat method with multiple sources.[16] Alternatively, the time-delay decorrelation method may be considered.[17,18] However, this approach is less convenient for signals in the microwave band, as the difficulty lies in constructing a time-delay line at microwave frequencies. In comparison, using another independent CSO or an active hydrogen maser as the reference oscillator to evaluate the performance of the device under test (DUT) remains a reliable solution. With the maturity of optical frequency division technology in recent years,[19,20] optically generated microwaves can inherit the exceptional frequency stability of

†Corresponding author. E-mail: zehuanglu@hust.edu.cn

© 2026 Chinese Physical Society and IOP Publishing Ltd. All rights, including for text and data mining, AI training, and similar technologies, are reserved.

ultra-stable lasers (USLs). Consequently, they can also serve as a frequency reference for measuring the frequency stability of CSOs.

As outlined above, the significant application value of CSOs has made their development, evaluation, and characterization key focuses in both academic and industrial research. This paper introduces the principles and experimental setup of the CSO, including the design of the microwave resonator, oscillation loop, and frequency-locking techniques. In the Results section, measurements of the CSO's frequency stability and phase noise are presented. To evaluate the frequency stability of the CSO, an optically generated microwave (OGM) based on optical frequency division is applied, which typically achieves stability on the order of 10^{-16} and phase noise of -105 dBc/Hz at 1 Hz in the X-band.[4,6,20–22] This setup meets the requirements for measuring the CSO's phase noise down to -95 dBc/Hz at 1 Hz.

Additionally, theoretical analysis and experimental verification of the CSO's noise sources are conducted, covering frequency-locking noise, microwave power fluctuation noise, temperature fluctuation noise, and 1.4 Hz vibrational noise from the pulse-tube cryocooler. By addressing these noise sources in future work, the frequency stability of the CSO system could be improved to the 10^{-16} level, with phase noise below -105 dBc/Hz at 1 Hz, comparable to that of the most advanced systems developed at the University of Western Australia (UWA) and the Franche-Comté Electronique Mécanique Thermique et Optique-Sciences et Technologies (FEMTO-ST).[1,2]

2. Experimental principles and setup

2.1. Frequency-locking principle of CSO

The core of the CSO is a sapphire-loaded copper cavity (SLC), which serves as the resonator and provides the foundation for its frequency stability. It selects the microwave signal resonant with a high-order whispering-gallery mode (WGM) of the sapphire cylinder in the X-band. Together with a low-noise amplifier (LNA) and a phase shifter, it forms an oscillation loop. By satisfying the Barkhausen criterion, it can generate a stable oscillating signal. The sapphire resonator acts as a frequency discriminator for the frequency-locked CSO. The microwave signal fed into the resonator, upon reflection, carries information that identifies the deviation between the resonant frequency and the oscillation frequency. The frequency-locking technique based on this concept was proposed by Pound and has since evolved into the Pound–Drever–Hall (PDH) technique for frequency stabilization of lasers.[23,24]

The application of the Pound frequency discrimination (PFD) technique in the CSO is illustrated in Fig. 1. Its principle can be described as follows: the carrier at frequency f_c, represented as $e^{i2\pi f_c t}$, undergoes frequency modulation with modulation depth φ_m and frequency f_m. Assuming a small modulation depth, this modulated signal can be approximated as a three-frequency wave, consisting of $J_0(\varphi_m)e^{i2\pi f_c t}$ and $J_1(\varphi_m)e^{i2\pi(f_c\pm f_m)t}$, where J_0 and J_1 are the expansion coefficients of the Bessel functions. Since the resonator linewidth Δf_0 is much smaller than f_m, the double sidebands at frequencies $f_c \pm f_m$ are fully reflected. Only the carrier at f_c interacts with the cavity and is partially reflected, expressed as $S_{11}(f_c)J_0 e^{i2\pi f_c t}$, where S_{11} is the reflection coefficient of the resonator. The reflected three-frequency wave is separated by a circulator and detected to obtain the raw error signal as

$$\begin{aligned} &\mathrm{Rerr} = -4\gamma_{\mathrm{PD}}P_{\mathrm{det}}J_0J_1\,\mathrm{Im}\,S_{11}(f_c)\cos(2\pi f_m t),\\ &S_{11}(f_c) = \frac{\beta_1 - 1 - i2Q\Delta f/f_0}{\beta_1 + 1 + i2Q\Delta f/f_0},\quad \Delta f = f_c - f_0. \end{aligned} \tag{1}$$

Here, γ_{PD} (mV/mW) and P_{det} represent the voltage conversion sensitivity and the detected power of the power detector (PD), respectively. S_{11} is characterized by the coupling coefficient β_1, quality factor Q, and resonant frequency f_0 of the sapphire cavity. In Eq. (1), the raw error signal can be extracted via demodulation techniques. With weak modulation ($\varphi_m \sim 0.1$), the approximation $J_0J_1 \approx \varphi_m/2$ can be applied, and the frequency-discriminator error signal is expressed as

$$\mathrm{Verr} = D_\nu(f_c - f_0),\quad D_\nu = -\frac{8\gamma_{\mathrm{PD}}P_{\mathrm{det}}\varphi_m\beta_1 Q}{(1+\beta_1)^2 f_0}, \tag{2}$$

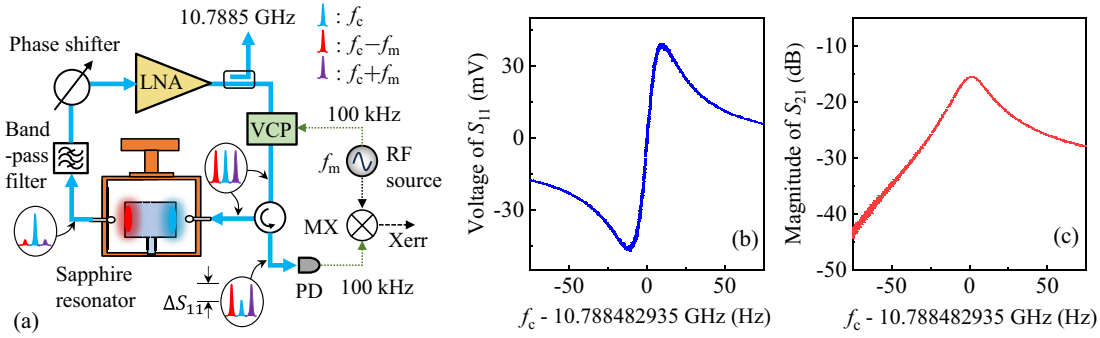


Fig. 1. (a) The scheme of the Pound frequency discrimination technique applied to a CSO. (b) The imaginary part of the S_{11} parameter is characterized by the voltage measured with a vector network analyzer. (c) The S_{21} parameter of the sapphire resonator, demonstrating a Q-factor reaching 5.1×10^8.

where D_v is the frequency-discrimination coefficient. In Fig. 1, the error signal can characterize the deviation between the oscillation frequency and the resonance center as $\mathrm{Im}S_{11}$. This signal is fed back by the servo controller to the voltage-controlled phase shifter (VCP) in the oscillation loop, thereby pulling the oscillation frequency to the resonance center.

2.2. The sapphire resonator

The sapphire cylinder with a diameter of 50 mm and a thickness of 30 mm is placed inside a copper cavity, with a pair of magnetic probes used to excite the $\mathrm{WGH}_{15,0,0}$ mode. In Fig. 1, the measurement of S_{21} by a vector network analyzer shows that the insertion loss is 15 dB. Despite this weak coupling causing a low coupling coefficient ($\beta_1 \approx 0.45$), it enables a high loaded Q-factor, reaching 5.1×10^8.

As analyzed in the phase noise model of a phase-locked oscillator,[7] the sapphire resonator serves as the frequency stabilizer of the oscillator. However, the frequency characteristics of the resonator are influenced by environmental factors, including temperature fluctuations, microwave power fluctuations, vibration, and mechanical deformation. Among these factors, the effects of the first two are noticeable, as demonstrated by the measurement illustrated in Fig. 2.

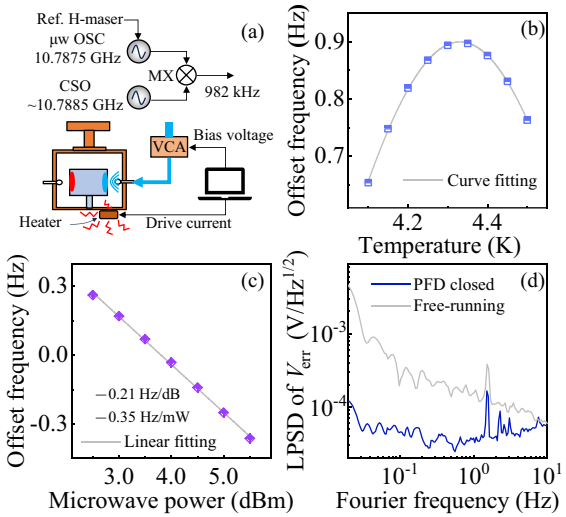


Fig. 2. (a) The scheme for measuring the frequency shift of the sapphire resonator by comparing it with a microwave signal source referenced to the hydrogen maser. (b) The measured frequency-temperature turning point. (c) The frequency shift at different power levels under operating conditions. (d) The linear power spectral density (LPSD) of the PFD error signal V_{err} under free-running and closed-loop conditions.

By scanning the surface temperature of the sapphire resonator or the microwave power fed into the cavity, corresponding shifts in its resonant frequency can be measured. A low-phase-noise signal generator (E8257D), referenced to an active hydrogen maser, provides a 10.7875 GHz signal as the frequency reference for measuring the microwave frequency of the CSO. Thus, the frequency shift is observed as a variation in the 986 kHz beat-note frequency.

The temperature-induced frequency shift is shown in Fig. 2(b). The temperature of the sapphire resonator is scanned from 3.6 K to 4.6 K, with a frequency-temperature turnover point T_{FTTP} observed at 4.330 K. By stabilizing the resonator at T_{FTTP} with a cryogenic temperature servo, the temperature fluctuation noise can be effectively suppressed. In Fig. 2(c), the microwave power fed into the resonator is varied by adjusting the bias voltage of a voltage-controlled attenuator (VCA), yielding a microwave power-induced frequency shift sensitivity of −0.35 Hz/mW.

To stabilize the microwave power, a directional coupler extracts 1/10 of the microwave power, which is converted into a voltage signal via a cryogenic PD (DT8012). This voltage is locked to a voltage reference in a low-noise controller (SIM960), thereby compensating for power fluctuation noise by adjusting the bias voltage of the VCA.

In the frequency-locking process, a 100 kHz modulated RF signal output from a lock-in amplifier (LIA) is applied to a VCP with a bandwidth of MHz, enabling the generation of a coherent three-frequency wave. After being reflected by the resonator, the signal is detected by a cryogenic PD, yielding a 100 kHz error signal synchronized with the modulation RF. After demodulation and amplification by the LIA, the error signal described by Eq. (2), $V(\Delta f) = AD_v\Delta f$, is obtained. Here, A is the gain provided by the LIA. By feeding this error signal back to the bias voltage of the VCP, the oscillation frequency is locked to the resonance center.

In Fig. 2(d), once the frequency lock is achieved, the fluctuation noise of the error signal is suppressed by almost one order of magnitude at Fourier frequencies below 1 Hz.

3. Frequency stability and phase noise

In this study, two CSOs were developed by the National Gravitation Laboratory (NGL) at Huazhong University of Science and Technology, designated as CSO-1 and CSO-2.[7] The frequency stabilities of CSO-1 measured with CSO-2, an H-maser, and an OGM are shown in Fig. 3(a). When compared with the OGM,[21] the Allan deviation of the relative frequency fluctuations reaches 2.1×10^{-15} at an averaging time of 70 s. Here, the frequency stability of the OGM is derived from a 30 cm Fabry–Pérot cavity with a stability of 1.9×10^{-16}.[25] A commercial frequency transmitter (Synchronization Technology Ltd, STW-FT series) is used to transmit the synthesized 100 MHz signal from CSO-1 to the distant laser lab. A commercial phase noise analyzer (PNA, Microchip 53100A) measures the 100 MHz signal derived from the OGM (9 GHz) via a 1/90 frequency divider, comparing it with the 100 MHz signal from CSO-1. For $\tau < 5$ s, the frequency stability is limited by the noise floor of the frequency transmitter, exhibiting a trend of $1 \times 10^{-14}\ \tau^{-1}$.

In addition, the frequency dividers also impose a limit on the short-term stability, with a single divider exhibiting a trend of $8 \times 10^{-15}\ \tau^{-1}$. This explains the observed short-term stability behavior of $2 \times 10^{-14}\ \tau^{-1}$. To accurately characterize

the short-term stability, a second oscillator (CSO-2) is used for this purpose, yielding an Allan deviation of 3.8×10^{-15} at 1 s.[7] However, for $\tau > 10$ s, the stability degrades rapidly due to the drift of CSO-2, which can be verified from the CSO-1 vs. H-maser comparison result.[3]

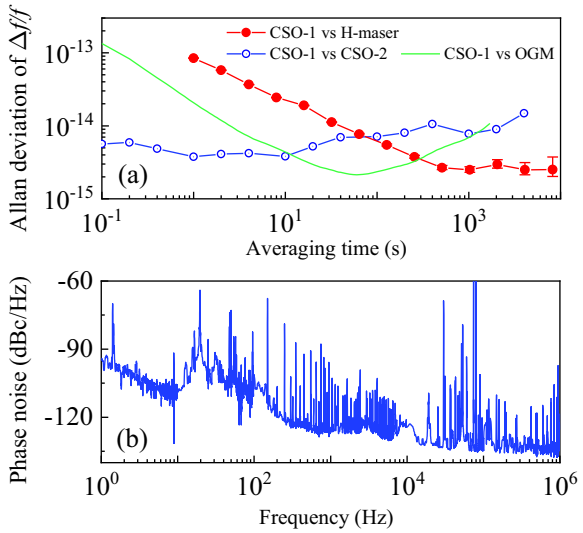


Fig. 3. (a) The frequency stabilities of CSO-1 are measured by comparison with CSO-2, an H-maser, and an OGM. (b) The phase noise of the 10.7885 GHz signal measured by comparing CSO-1 with CSO-2.

For Fourier frequencies above 1 Hz, the phase noise of CSO-1 is measured as shown in Fig. 3(b). The close-in phase noise of the 10.7885 GHz microwave signal reaches −95 dBc/Hz at 1 Hz and −125 dBc/Hz at 1 kHz. It can potentially be improved by employing a lower-phase-noise amplifier.[26] Above 10 Hz, ripples are present in the phase noise spectrum, arising partly from high-frequency vibrations of the cryocooler and partly from ripple noise coupled through the bias supplies of the LNA and VCP. In the frequency range above 10 kHz, the phase noise exhibits a white noise floor, reaching −135 dBc/Hz from 10 kHz to 1 MHz. This is due to the weak microwave power returned to the LNA. In principle, the high-frequency phase noise can be reduced by lowering the insertion loss of the resonator. Additionally, low-noise filtering techniques can also be implemented for this purpose.[3]

4. Noise analysis

A free-running CSO already exhibits frequency stability at the 10^{-14} level. Only under optimal locking conditions can the frequency stability of its output signal approach that of the resonator itself, potentially reaching the regime of 10^{-15} to 10^{-16}. According to the noise model of a phase-locked CSO,[7] the primary noise contributions originate from two categories: frequency-locking noise and resonator frequency noise. Frequency-locking noise is typically introduced during the demodulation process of the LIA, including the intrinsic electronic noise of the demodulator and residual amplitude modulation (RAM) noise from the modulator.[27] The sources of resonator frequency noise are diverse. Typical contributors include temperature fluctuation noise, microwave power fluctuation noise, and vibrational noise from the cryocooler. These noises are analyzed in detail below.

4.1. Frequency-locking noise

In Eq. (2), the front-end detection voltage noise $n_{\rm PFD}$ introduced by the PFD technique aliases with the error voltage $V_{\rm err}$, thereby manifesting as frequency-locking noise. Since the PFD technique employs high-frequency modulation and demodulation, the predominant component of the introduced voltage noise originates from the high-frequency white noise of the detector. Consequently, the contribution of frequency-locking noise to the relative frequency stability can be expressed as

$$\sigma_y(\tau) = \frac{(1+\beta_1)\,h_{\rm PFD}}{8\sqrt{2}V_{\rm PD}\beta_1\varphi_{\rm m}Q_{\rm L}}\cdot\frac{1}{\sqrt{\tau}}, \tag{3}$$

where β_1, $Q_{\rm L}$, $V_{\rm PD}$, $\varphi_{\rm m}$, and $h_{\rm PFD}$ denote the coupling coefficient at the SLC input port, the loaded Q-factor, the voltage detected by the PD in the PFD technique, the phase modulation depth, and the white noise component of the PFD, respectively.

The $h_{\rm PFD}$ mainly originates from the inherent noise of the LIA, including the output noise $n_{\rm out}$ and demodulation noise $n_{\rm DM}$. The relationship between them can be expressed as $n_{\rm lim} = (n_{\rm DM} \oplus n_{\rm out})/A$, $h_{\rm PFD} \equiv n_{\rm lim}$, where $n_{\rm lim}$ and A are the noise limit and the sensitivity gain factor of the LIA, respectively. By connecting a 50 Ω termination to the input of the LIA (SR830) and collecting the voltage noise from its X output channel, the output voltage noise $n_{\rm out}$ of the LIA can be characterized. Under different gain settings, the output voltage noise of the LIA remains nearly identical, exhibiting a $1/f$-type voltage noise of $1.3\times10^{-6}\ ({\rm Hz/f})^{1/2}{\rm V}/\sqrt{\rm Hz}$ at low frequencies.

To measure the demodulation noise $n_{\rm DM}$, a weak modulation signal (100 kHz, 4 mV) generated by the LIA itself is fed back into its input port for demodulation. When demodulating in-phase, the modulation signal is detected and amplified at the X channel. When demodulating in quadrature, the voltage noise from the Y channel represents the demodulation noise, as presented in Fig. 4(a). As the gain factor increases, the demodulation noise $n_{\rm DM}$ decreases. At a gain factor of 10000, the limiting voltage $h_{\rm PFD}$ as low as 4 nV/$\sqrt{\rm Hz}$ can be detected. Based on Eq. (3), the LIA's detection limit for the frequency stability is shown in Fig. 4(b), reaching $4\times10^{-16}/\sqrt{\tau}$ at $0.01\sim1$ s with a gain factor of 10000.

To reduce the frequency-locking noise, one can increase the frequency-discrimination coefficient D_V or enhance the gain factor A at the detection front-end. With a phase modulation depth $\varphi_{\rm m} = 0.1$ and a loaded Q-factor $Q_{\rm L} = 5.1\times10^8$, the trend of D_V as a function of the power fed into the SLC

is shown in Fig. 4(c). As the power increases from −10 dBm to −2 dBm, D_ν correspondingly increases from 0.4 mV/Hz to 4.2 mV/Hz.

In Fig. 4(c), prior to optimization, CSO-1 operated in a high-power mode with a D_ν of 11.8 mV/Hz and a gain factor of 500. The results indicated that the contributed short-term stability of $h_{\rm PFD}$ is $3\times10^{-15}/\sqrt{\tau}$. After optimization, operating in a low-power mode, the D_ν is only 2 mV/Hz, but the gain factor is increased to 5000. The results show that the contribution of $h_{\rm PFD}$ is reduced to $4\times10^{-16}/\sqrt{\tau}$, reaching 2×10^{-16} at averaging times from 10 s to 1000 s.

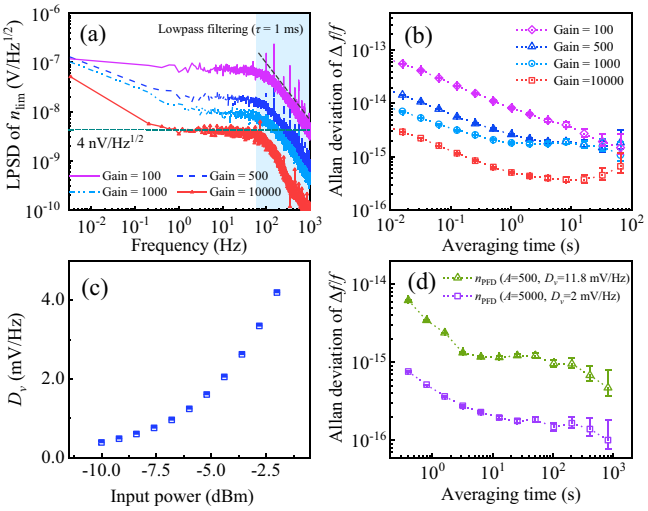


Fig. 4. (a) The limiting voltage noise $n_{\rm lim}$ detected by the PFD technique. (b) The LIA's intrinsic noise contribution to frequency stability. (c) The frequency-discrimination coefficients under different input powers. (d) The contribution of the PFD technique's locking noise to frequency stability. Before optimization, $A=500$, $D_\nu=11.8$ mV/Hz; after optimization, $A=5000$, $D_\nu=2$ mV/Hz.

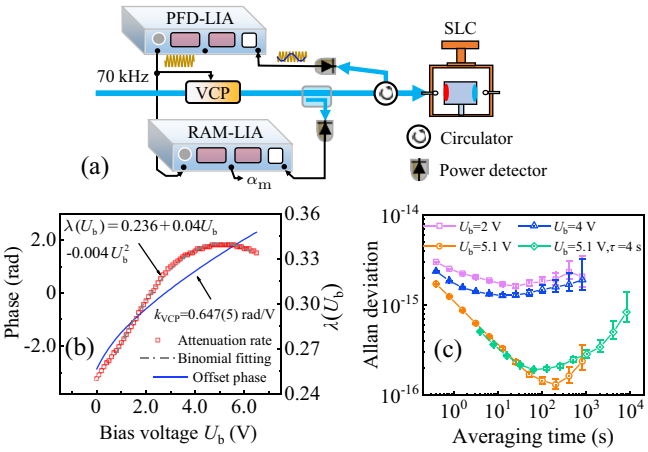


Fig. 5. (a) The scheme for measuring RAM noise. (b) The attenuation and phase shift of the VCP with changes in the bias voltage $U_{\rm b}$. The attenuation turning point is 5.1 V, and the phase-shift sensitivity $k_{\rm VCP}$ is 0.647 rad/V. (c) The contribution of RAM noise to frequency stability under different bias voltages.

4.2. Residual amplitude modulation noise

In the PFD technique, a VCP is required to perform phase modulation (PM). However, due to the non-uniform loss of the VCP, a concomitant amplitude modulation (AM) at the same frequency, denoted as $\alpha_{\rm m}$, is introduced. The AM component is demodulated by the LIA and converted into an offset voltage, thereby affecting the frequency detection. This effect is known as residual amplitude modulation (RAM) noise. According to Eq. (1), the detected error signal with the RAM term is given by $\mathrm{Verr}=D_\nu\,(f_{\rm RAM}+\delta f)$, where $\delta f=f_{\rm c}-f_0$ represents the deviation between the carrier and resonance frequencies. The frequency offset around the locking point, referred to as the RAM frequency, is expressed as

$$f_{\rm RAM}=\left(\beta_{\rm I}^2-1\right)f_0\alpha_{\rm m}/4\beta_{\rm I}Q\varphi_{\rm m}. \tag{4}$$

Here $f_{\rm RAM}$ carries the same weight as the identified frequency deviation δf, thus limiting the long-term stability of frequency locking in the PFD scheme. Furthermore, $f_{\rm RAM}$ acts as a conduit, thereby coupling the microwave power noise $n_{\rm P}$ into the front end of the frequency discrimination scheme, expressed as $D_\nu f_{\rm RAM}n_{\rm P}$.

An effective method to reduce RAM noise is shown in Fig. 5(b). The insertion-loss turning point of the VCP is used to suppress amplitude modulation. With the modulation voltage $U_{\rm m}$ applied to the VCP, the amplitude modulation can be expressed as $\alpha_{\rm m}=\dot\lambda(U_{\rm b})/\lambda(U_{\rm b})\cdot U_{\rm m}$, thus $\delta\alpha_{\rm m}=U_{\rm m}\ddot\lambda/\lambda\cdot\delta U_{\rm b}$, $\dot\lambda(U_{\rm b})=0$, and the $\boldsymbol{E}(\alpha_{\rm m})=0$. Here, $U_{\rm b}$ is the bias voltage, $\dot\lambda$ and $\ddot\lambda$ represent the first and second derivatives of the attenuation coefficient with respect to bias voltage.

In Fig. 5(b), with a modulation voltage $U_{\rm m}$ of 0.1 V and the fitted λ, the contribution of the bias voltage noise $\delta U_{\rm b}$ to $\delta\alpha_{\rm m}$ is merely 0.24%. From the expression for $f_{\rm RAM}$, the transfer coefficient from $\delta\alpha_{\rm m}$ is 154 Hz/unit. Thus, the conversion coefficient from the bias voltage fluctuation $\delta U_{\rm b}$ to $f_{\rm RAM}$ is 0.37 Hz/V. The typical $\delta U_{\rm b}$ is characterized by a $1/f$ behavior in the close-in frequency range, achieving a level of 5 $\mu\mathrm{V}/\sqrt{\mathrm{Hz}}$ at 1 Hz for a 5 V bias, which is ensured by the voltage reference module (SRS SIM960). Thus, the predicted contribution to frequency stability is 1.7×10^{-16}.

The scheme in Fig. 5(a) is designed to measure RAM noise. It requires two LIAs. One is employed for the PFD technique, and the other is used to measure the RAM noise. The two LIAs are synchronized with respect to the 100 Hz modulation signal. After demodulation, the voltage characterizing the amplitude modulation is given by $u=2\alpha_{\rm m}\gamma_{\rm D}P_{\rm det}$, where $\gamma_{\rm D}$ is the detection efficiency of the PD, and $P_{\rm det}$ is the detected microwave power. The RAM noise can be expressed as

$$\sigma_y^{\rm RAM}=\frac{\beta_{\rm I}^2-1}{4\beta_{\rm I}Q\varphi_{\rm m}P_{\rm det}\gamma_{\rm D}G_{\rm LA}}\sigma_u. \tag{5}$$

Here, σ_u and $G_{\rm LA}$ are the Allan deviation of the output voltage from the RAM-LIA and its gain factor, respectively.

The measured RAM noise is shown in Fig. 5(c). When the bias voltage $U_{\rm b}$ of the VCP is set to 2 V and 4 V, the measured RAM noise is on the order of 10^{-15}. When $U_{\rm b}$ is set

to the turning point (5.1 V), the measured RAM noise is notably suppressed. For averaging times between 1–50 s, the stability follows a trend of $1\times10^{-15}/\sqrt{\tau}$, reaching a floor of 1.3×10^{-16} at 200 s. Increasing the sampling interval to 4 s, the measured floor reaches 2.0×10^{-16} at 100 s, which aligns with the predicted result.

In Fig. 5(a), the RAM-LIA also measures the intrinsic voltage noise of the PD.[27] In principle, only the high-frequency white noise within the PD affects the measurement, expressed as

$$\sigma_y^{\mathrm{RAM,PD}}=\frac{\beta_1^2-1}{4\beta_1 Q\varphi_{\mathrm{m}}}\cdot\sqrt{\frac{k_{\mathrm{B}}T}{P_{\mathrm{det}}\tau}}. \tag{6}$$

Here, $k_{\mathrm{B}}=1.38\times10^{-23}$ J/K is the Boltzmann constant, and the operating temperature T is 300 K. In Eq. (6), the calculated noise floor is $1.3\times10^{-15}/\sqrt{\tau}$, which is consistent with the results shown in Fig. 5(c). The results agree with the intuitive understanding that RAM noise essentially stems from the coupling of carrier amplitude noise into the PFD noise, manifesting as a limitation over longer periods.

4.3. Temperature fluctuation noise

To precisely stabilize the resonator temperature at FTTP, the measurement scheme shown in Fig. 2(a) is employed to determine the resonant frequency. The relationship between the resonant frequency and temperature can be obtained via curve fitting. At FTTP, the conversion between temperature fluctuations and the relative change in resonant frequency can be expressed as

$$\sigma_y=\frac{1}{f_0}\frac{\partial^2 f_0}{\partial T^2}\Delta T_{\mathrm{FTTP}}\sigma_T. \tag{7}$$

Here, $f_0^{-1}\cdot\partial^2 f_0/\partial T^2$ is the second derivative of frequency with respect to temperature, with a value of 1×10^{-9} Hz/K^2, and ΔT_{FTTP} is the uncertainty of the measured FTTP.[7]

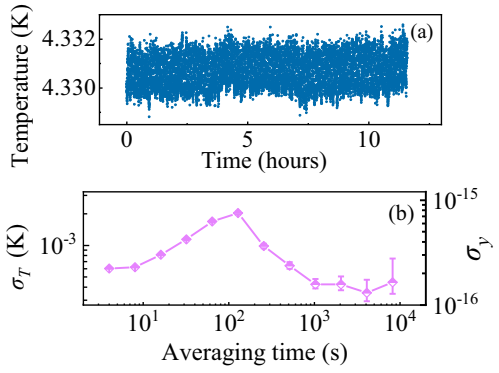


Fig. 6. (a) The temperature of the sapphire resonator is monitored by an independent temperature sensor for 11.5 hours. (b) The Allan deviation of temperature fluctuation and its contribution to frequency stability.

According to the scheme in Fig. 2(a), the frequency reference is supplied by a hydrogen maser. The uncertainty of the measured frequency can be reduced to 100 μHz when each measurement is averaged over 5 minutes. The accuracy of temperature measurement is ensured by the temperature sensor (Cernox$^{\mathrm{TM}}$), which has a temperature resolution of 89 μK at 4.2 K. By performing peak fitting on the measurement curve in Fig. 2(b), the FTTP can be determined with a fitting uncertainty of 3 mK. Thus, ΔT_{FTTP} can be reduced to 4 mK.

The temperature of the resonator is measured by an independent temperature sensor. In Fig. 6(a), over a period of one day, the peak-to-peak temperature fluctuation remains within 3 mK. According to Eq. (7), the temperature fluctuation noise can be converted into the contribution to frequency stability, as presented in Fig. 6(b). For averaging times from 1 to 1000 s, the contribution of the temperature fluctuation is on the order of 10^{-16}.

4.4. Microwave power fluctuation noise

In the power servo, part of the microwave power is coupled and converted into a voltage signal by the PD. The fluctuation of the voltage signal can be considered to be caused by the relative intensity noise (RIN) of the microwave signal. The signal is fed back to the VCA after passing through the PI controller, realizing compensation of the RIN. Such a design relies on a crucial assumption: the coupled power and the main power are correlated.

The principle of the power servo is illustrated in Fig. 7(a). A signal source (E8257D) generates the microwave signal under test at 10.8 GHz. The VCA acts as the actuator by adjusting the attenuation according to the applied bias voltage. The power splitter divides the test signal into two paths: one serves as the sensing branch for the power servo loop, and the other acts as the monitor branch for the main power. Both branches are connected to identical PDs. The Data Acquisition (DAQ) unit simultaneously samples the voltages from both paths. The acquired voltage signals are calculated to characterize the correlation between the sensing branch and the main power branch.

The voltage samples obtained by the two PDs are V_{s} and V_{d}, respectively, and their intrinsic detection noises n_{PD} of the two PDs are uncorrelated. Their cross-spectra satisfy the condition $|S_{\mathrm{sd}}(f)|^2<S_{\mathrm{s}}(f)\cdot S_{\mathrm{d}}(f)$. The coherence coefficient between the two sets of voltage samples can be defined as

$$\gamma_{\mathrm{sd}}^2(f)<\frac{|S_{\mathrm{sd}}(f)|^2}{S_{\mathrm{s}}(f)\cdot S_{\mathrm{d}}(f)}. \tag{8}$$

The extinction of the coherence coefficient γ_{sd}^2 is inevitable due to the inherent noise of the detector. The γ_{sd}^2 can directly characterize the effective bandwidth of the power servo.

Two independent PDs (DT8012) are employed to analyze the power coherence between the inner and outer loops of the power servo. In Fig. 7(c), the coherence coefficients γ_{sd}^2 under different detection powers are measured. When the detected

power is −14 dBm, the coherence bandwidth ($\gamma^2_{sd} > 0.6$) of the two PDs is only 1 Hz. On the other hand, when the detected power is −18 dBm, the coherence bandwidth is significantly enhanced, reaching 10 Hz.

The RIN of the microwave signal coupled into the sensing branch is suppressed when the power servo is enabled. The in-loop power (P_s) noise reduction is characterized by the out-of-loop detected power (P_d). It achieves a gain of $\alpha\eta_{PD}G_{PI}$, where α is the attenuation and G_{PI} is the gain of the PI controller.

Figure 7(b) shows the RIN of the out-of-loop microwave power. When the detected power is set to −14 dBm, the poor correlation between the inner and outer loops results in the RIN being even higher than that in the open-loop case. At a power level of −18 dBm, the RIN is effectively suppressed, indicating that the power servo is functioning properly.

The front-end noise in the power servo arises from the reference voltage V_{ref} and the intrinsic noise of the PD (n_{PD}). With the measured microwave power-induced frequency sensitivity (−0.21 Hz/dB) and the conversion efficiency of the PD (21 mV/dB at −18 dBm), an estimation of the fundamental limit that RIN noise places on frequency stability is shown in Fig. 7(d). In the short term, the limit of the RIN on the stability is 5.5×10^{-16}, which is constrained by flicker frequency noise converted from the $1/f$-type noise of the reference voltage. For averaging times exceeding 1000 s, the RIN begins to degrade, which is due to random walk and drift of the reference voltage.

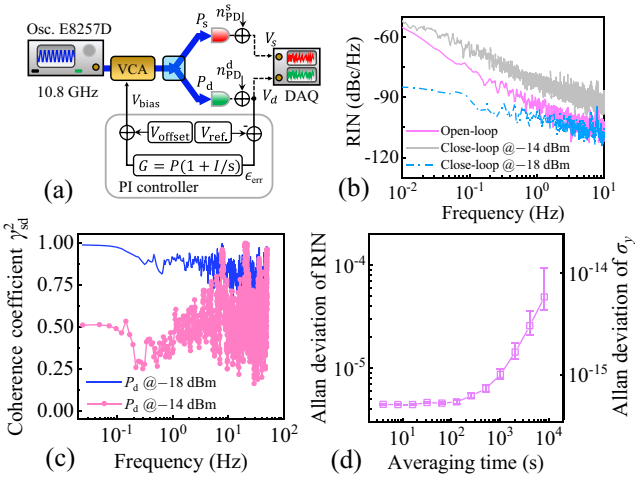


Fig. 7. (a) The measurement scheme for validating the effectiveness of the microwave power servo. (b) The RIN of the microwave power under open-loop and closed-loop conditions. (c) The coherence coefficient of the detected voltage from the out-of-loop path of the microwave power servo at test points of −18 dBm and −14 dBm. (d) The Allan deviation of the RIN and the estimated contribution to frequency stability.

4.5. 1.4 Hz vibration-induced noise

The sapphire resonator is mounted on the 4 K cold plate. Vibrational noise from the pulsetube cryocooler causes variations in the relative position between the microwave probe and the sapphire cylinder. It affects the excitation of the WGH mode, causing variations in the resonant frequency, coupling coefficient, and Q-factor. A prominent feature is the 1.4 Hz pulsed vibration signal, which manifests in the phase noise spectrum of the CSO or in the in-loop noise spectrum of the PFD technique, as shown in Fig. 2(d).

In Fig. 8(a), the phase noise spectrum of the CSO is zoomed in near 1.4 Hz, and two frequency components can be observed, which originate from the vibrational noise of two independent cryocoolers. Two distinct vibration signals are observable at 1.41 Hz and 1.44 Hz, originating from CSO-1 and CSO-2, respectively. Their contributions to the phase noise spectrum in terms of power and bandwidth are −70 dBc/Hz with a 0.02 Hz bandwidth and −79 dBc/Hz with a 0.03 Hz bandwidth, respectively.

The phase noise S_φ introduced by the two vibration signals contributes to the frequency stability, which can be calculated as follows:

$$\sigma_y^2(\tau) = \frac{1}{f_0^2}\int_0^\infty 2f^2 S_\varphi(f)\frac{\sin^4(\pi\tau f)}{(\pi\tau f)^2}\,\mathrm{d}f. \tag{9}$$

In Fig. 8(b), the calculated contributions of the two vibration signals to the frequency stability are $2.5 \times 10^{-15}\ \tau^{-1}$ and $1.2 \times 10^{-15}\ \tau^{-1}$, respectively. These contributions constitute a limiting factor for the short-term frequency stability but decrease rapidly with increasing averaging times.

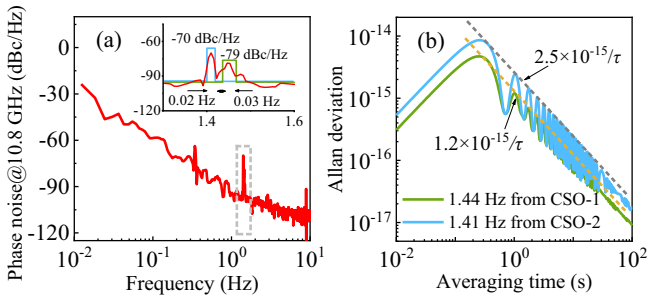


Fig. 8. (a) The zoomed phase noise spectrum showing the identifiable 1.4 Hz vibration noise. (b) The contribution of the 1.4 Hz vibration noise to frequency stability.

5. Discussion

Figure 9 summarizes the main noise contributions to CSO-1, determining the current-limited frequency stability. In the short term, the main contributor is the 1.4 Hz vibration noise unique to the pulse-tube cryocooler. Although its contribution in the time domain follows a τ^{-1} decay trend, it limits the frequency stability at the second scale. It can be improved by an assembly with lower vibration sensitivity or by using a cryocooler with lower vibration noise.[28] In the future, mitigating this noise could break the barrier preventing the 1-second frequency stability from reaching the E-16 level.

By optimizing the frequency-discrimination coefficient and the front-end gain factor of the LIA, the frequency-locking noise is effectively reduced, reaching $4 \times 10^{-16}/\sqrt{\tau}$ at 0.4–2 s, as shown in Fig. 4(d). However, it does not decrease with

longer averaging times because the frequency-locking noise also includes the output noise of the LIA and the RAM noise, which manifest as a floor of 2×10^{-16} for $\tau>2$ s.

For averaging times between 2–200 s, temperature fluctuation noise and microwave power fluctuation noise become the dominant noise sources in CSO-1. Their combined contribution lies in the range of 6×10^{-16} to 1×10^{-15}, which limits the frequency stability from reaching 10^{-16}. Notably, at an averaging time of 140 s, the temperature fluctuation noise manifests as a hump in the Allan deviation plot. This is attributable to the time constant of the temperature feedback loop. For the temperature monitor outside the loop, only temperature fluctuations with averaging times greater than 200 s can be measured for effective compensation. This problem can be mitigated by performing thermal conduction simulations to identify optimal sensing or control locations and to tailor the temperature control scheme for the sapphire cavity.

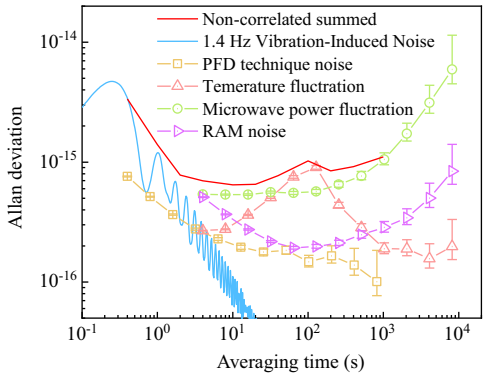


Fig. 9. The main noise contributions in CSO-1 are converted into contributions to frequency stability. The total contribution, shown as the red curve, is calculated by an uncorrelated squared summation of individual noise contributions.

For averaging times beyond 200 s, power fluctuation noise rises and becomes the dominant limit to frequency stability. This originates from locking the microwave power to the controller's voltage reference — a noise source that is inherently difficult to suppress. Because the voltage reference noise shows $1/f$ characteristics near 1 Hz, it typically appears as random-walk noise and drift at lower frequencies, thereby translating into resonant frequency drift. To mitigate this, one could lock the microwave power to a voltage reference with better long-term stability or operate at the power-induced frequency-shift turnover point. This scheme allows the CSO to maintain frequency stability at the 10^{-16} level, even over medium-to-long averaging times.[29]

6. Conclusion

In the frequency-locked CSO-1, the PFD locking noise is optimized, reaching $4\times10^{-16}/\sqrt{\tau}$ at 0.4–2 s. However, its performance will not be maintained for longer averaging times due to the RAM noise; a noise floor of 2×10^{-16} is achieved at 100 s. For averaging times beyond 200 s, the voltage reference in the microwave power servo becomes susceptible to random walk or drift, thus limiting the CSO-1's frequency instability to levels above 10^{-16}. In the future, it is necessary to optimize the assembly of the sapphire resonator to reduce the effect of 1.4 Hz vibrational noise on PFD locking noise in the short term. Effective monitoring of the sapphire resonator's temperature fluctuations is required, as it constitutes the primary barrier preventing CSO-1 from reaching a stability of 10^{-16}. A more stable voltage reference is also required, both to suppress the RAM noise and to ensure the long-term stability of the microwave power.

Acknowledgment

Project supported by the National Key Research and Development Program of China (Grant No. 2022YFB3904002).

References

[1] Hartnett J G and Nand N R 2010 *IEEE Trans. Microwave Theory Tech.* **58** 5617322
[2] Fluhr C, Grop S, Dubois B, Kersalé Y, Rubiola E and Giordano V 2016 *IEEE Trans. Ultrason. Ferroelectr. Freq. Control* **63** 915
[3] Zhong E, Zheng Y, Hong J, Liu M, Luo Y, Liu H, Deng K, Zhang J and Lu Z 2025 *Rev. Sci. Instrum.* **96** 064711
[4] Xie X, Bouchand R, Nicolodi D, Giunta M, Hänsel W, Lezius M, Joshi A, Datta S, Alexandre C, Lours M, Tremblin P A, Santarelli G, Holzwarth R and Le Coq Y 2017 *Nat. Photonics* **11** 44
[5] Yan L L, Zhao W Y, Zhang Y Y, Tai Z Y, Zhang P, Rao B J, Ning K, Zhang X F, Guo W G, Zhang S G and Jiang H F 2018 *Chin. Phys. B* **27** 030601
[6] Yan L, Ruan J, Zhang P, Rao B, Li M, Du Z and Zhang S 2025 *Photonics* **12** 153
[7] Zhong E, Le Floch J M, Liu H, Deng K, Zhang J and Lu Z 2025 *IEEE Access* **13** 110813
[8] Santarelli G, Audoin C, Makdissi A, Laurent P, Dick G J and Clairon A 1998 *IEEE Trans. Ultrason. Ferroelectr. Freq. Control* **45** 887
[9] Lipphardt B, Gerginov V and Weyers S 2017 *IEEE Trans. Ultrason. Ferroelectr. Freq. Control* **64** 761
[10] Guéna J, Rosenbusch P, Laurent P, Abgrall M, Rovera D, Santarelli G, Tobar M E, Bize S and Clairon A 2010 *IEEE Trans. Ultrason. Ferroelectr. Freq. Control* **57** 647
[11] Mann A G, Giles A J, Blair D G and Buckingham M J 1992 *J. Phys. D: Appl. Phys.* **25** 1105
[12] Doeleman S, Mai T, Rogers A E E, Hartnett J G, Tobar M E and Nand N 2011 *Publ. Astron. Soc. Pac.* **123** 582
[13] Tan T R, Navickas T, Valahu C, Jee J, Rao A, Millican M and Biercuk M 2023 *2023 Joint Conference of the European Frequency and Time Forum and IEEE International Frequency Control Symposium (EFTF/IFCS)* (Toyama, Japan: IEEE) pp.1–2
[14] Nagel M, Parker S R, Kovalchuk E V, Stanwix P L, Hartnett J G, Ivanov E N, Peters A and Tobar M E 2015 *Nat. Commun.* **6** 8174
[15] Campbell W M, McAllister B T, Goryachev M, Ivanov E N and Tobar M E 2021 *Phys. Rev. Lett.* **126** 071301
[16] Fluhr C, Dubois B, Tetu G L, Soumann V, Paris J, Rubiola E and Giordano V 2022 *IEEE Trans. Instrum. Meas.* **72** 1005408
[17] Pang Z, Li C, Dai H, Li W, Song D, Meng F, Lin Y and Wang B 2026 *Laser Photonics Rev.* **20** e01773
[18] Rubiola E, Salik E, Huang S, Yu N and Maleki L 2005 *J. Opt. Soc. Am. B* **22** 987
[19] Yao Y, Jiang Y, Yu H, Bi Z and Ma L 2016 *Natl. Sci. Rev.* **3** 463
[20] Nakamura T, Davila-Rodriguez J, Leopardi H, Sherman J A, Fortier T M, Xie X, Campbell J C, McGrew W F, Zhang X, Hassan Y S, Nicolodi D, Beloy K, Ludlow A D, Diddams S A and Quinlan F 2020 *Science* **368** 889

[21] Zheng Y, Liu M, Zhong E, Pang L, Wang Z, Wu Q, Wei Q, Liu H, Zhang J and Liu M 2026 *J. Time Freq.* (submitted)
[22] Nardelli N V, Fortier T M, Pomponio M, Baumann E, Nelson C, Schibli T R and Hati A 2022 *APL Photonics* **7** 026105
[23] Pound R V 1946 *Rev. Sci. Instrum.* **17** 490
[24] Drever R W P, Hall J L, Kowalski F V, Hough J, Ford G M, Munley A J and Ward H 1983 *Appl. Phys. B* **31** 97
[25] Wang Z, Ma Z, Wei W, Chang J, Zhang J, Wu Q, Yuan W, Deng K, Lu Z and Zhang J 2024 *Rev. Sci. Instrum.* **95** 053002
[26] Leeson D B 1966 *Proc. IEEE* **54** 329
[27] Locke C R, Ivanov E N, Hartnett J G, Stanwix P L and Tobar M E 2008 *Rev. Sci. Instrum.* **79** 051301
[28] Zhang J, Wang Z, Wei Q, Chang J, Wu Q, Chen X, Yuan W, Deng K, Lu Z and Zhang J 2025 *Rev. Sci. Instrum.* **96** 053002
[29] Giordano V, Grop S, Bourgeois P Y, Kersalé Y and Rubiola E 2014 *J. Appl. Phys.* **116** 054901